CAMBRIDGE
UNIVERSITY PRESS

Research Paper

PKS 2250–351: A giant radio galaxy in Abell 3936

N. Seymour[1], M. Huynh[2,3], S. S. Shabala[4], J. Rogers[4], L. J. M. Davies[3], R. J. Turner[4], A. O'Brien[5], C. H. Ishwara-Chandra[6], J. E. Thorne[3], T. J. Galvin[2], T. Jarrett[7], H. Andernach[8], C. Anderson[2], J. Bunton[5], K. Chow[5], J. D. Collier[9,10], S. Driver[3], M. D. Filipovic[9], G. Gürkan[2], A. M. Hopkins[11], A. D. Kapińska[12], D. A. Leahy[13], J. Marvil[12], P. Manojlovic[5,10], R. P. Norris[5,10], C. Phillips[5], A. Robotham[3], L. Rudnick[14], V. Singh[15] and S. V. White[1,16]

[1]International Centre for Radio Astronomy Research, Curtin University, Bentley, WA 6102, Australia, [2]CSIRO Astronomy and Space Science, 26 Dick Perry Avenue, Kensington, WA 6151, Australia, [3]International Centre for Radio Astronomy Research, M468, University of Western Australia, Crawley, WA 6009, Australia, [4]School of Natural Sciences, University of Tasmania, Private Bag 37, Hobart, TAS 7001, Australia, [5]CSIRO Astronomy and Space Science, P.O. Box 76, Epping, NSW 1710, Australia, [6]National Centre for Radio Astrophysics, TIFR, Post Bag No. 3, Ganeshkhind Post, 411007 Pune, India, [7]Astronomy Department, University of Cape Town, Private Bag X3, Rondebosch 7701, South Africa, [8]Departamento de Astronomía, DCNE, Universidad de Guanajuato, Apdo. Postal 144, Guanajuato, CP 36000, Gto., Mexico, [9]Department of Astronomy, The Inter-University Institute for Data Intensive Astronomy (IDIA), University of Cape Town, Rondebosch 7701, South Africa, [10]School of Computing, Engineering and Mathematics, Western Sydney University, Locked Bag 1797, Penrith, NSW 2751, Australia, [11]Faculty of Science and Engineering, Australian Astronomical Optics, AAO-Macquarie, Macquarie University, 105 Delhi Road, North Ryde, NSW 2113, Australia, [12]National Radio Astronomy Observatory, 1003 Lopezville Road, Socorro, NM 87801, USA, [13]Department of Physics and Astronomy, University of Calgary, Calgary, Alberta, T2N 1N4, Canada, [14]School of Physics and Astronomy, Minnesota Institute for Astrophysics, University of Minnesota, 116 Church Street SE, Minneapolis, MN 55455, USA, [15]Astronomy and Astrophysics Division, Physical Research Laboratory, Ahmedabad 380009, India and [16]Department of Physics and Electronics, Rhodes University, P.O. Box 94, 6140 Grahamstown, South Africa

Abstract

We present a detailed analysis of the radio galaxy PKS 2250−351, a giant of 1.2 Mpc projected size, its host galaxy, and its environment. We use radio data from the Murchison Widefield Array, the upgraded Giant Metre-wavelength Radio Telescope, the Australian Square Kilometre Array Pathfinder, and the Australia Telescope Compact Array to model the jet power and age. Optical and IR data come from the Galaxy And Mass Assembly (GAMA) survey and provide information on the host galaxy and environment. GAMA spectroscopy confirms that PKS 2250−351 lies at $z = 0.2115$ in the irregular, and likely unrelaxed, cluster Abell 3936. We find its host is a massive, 'red and dead' elliptical galaxy with negligible star formation but with a highly obscured active galactic nucleus dominating the mid-IR emission. Assuming it lies on the local $M-\sigma$ relation, it has an Eddington accretion rate of $\lambda_{EDD} \sim 0.014$. We find that the lobe-derived jet power (a time-averaged measure) is an order of magnitude greater than the hotspot-derived jet power (an instantaneous measure). We propose that over the lifetime of the observed radio emission ($\sim$300 Myr), the accretion has switched from an inefficient advection-dominated mode to a thin disc efficient mode, consistent with the decrease in jet power. We also suggest that the asymmetric radio morphology is due to its environment, with the host of PKS 2250−351 lying to the west of the densest concentration of galaxies in Abell 3936.

Keywords: galaxies: active – radio continuum: galaxies

1. Introduction

Radio-loud active galactic nuclei (AGN) are one manifestation of the supermassive black holes (SMBHs, 10^5–10^9 M$_\odot$) which lie at the centre of nearly all galaxies. They are powered by bipolar relativistic outflows (i.e. jets) of ionised material originating close to the SMBH (Rees 1978). In the local Universe, radio-loud AGN are typically hosted by passive elliptical galaxies with negligible accretion rates (Eddington ratio < 1%, see Heckman & Best 2014, and below). However, many of the most powerful radio-loud AGN in

the distant Universe are powered by SMBH with very high accretion rates (e.g. Drouart et al. 2014). This difference is thought to be due to differing natures of the accretion disc at high and low accretion rates. Typically, these rates are normalised to the theoretical maximum accretion rate (the 'Eddington' rate, $\lambda_{EDD} = 1$). By comparison to stellar mass black holes in our own galaxy (Merloni, Heinz, & di Matteo 2003; Fender, Belloni, & Gallo 2004; McHardy et al. 2006), SMBHs with low Eddington accretion rates, $\lambda_{EDD} \leq 0.01$, are thought to have a thick disc, efficient at producing jets whereas SMBHs with high Eddington accretion rates, $\lambda_{EDD} > 0.01$, are thought to have a thin disc (TD) which is less efficient at producing jets. However, both states of accretion disc can produce jets with powers proportional to the SMBH mass, spin, and accretion (Meier 2002). However, converting from the observed radio luminosity to jet power is complex and involves taking into account the environment of the AGN (e.g. Krause et al. 2019).

Giant radio galaxies (GRGs) are a rare class of radio-loud AGN with projected maximum angular extents > 1 Mpc of which only

a few hundred are known (Kuźmicz et al. 2018, and references therein). It is unusual for radio sources to grow so large as it presumably requires a low enough density in the local intergalactic medium (IGM) to travel far, but a high enough density that the observed jets have something to work against, thereby creating 'hotspots' where the jets terminate against the IGM. Giant radio sources are believed to be the late stage in the evolution of otherwise normal radio galaxies such as Cygnus A (Ishwara-Chandra & Saikia 1999). If this is true then there must be many more giant radio sources than known today, but are missed due to observational selection effects. Komberg and Pashchenko (2009) have shown that GRGs are no different to the population of less extended radio-loud AGN in terms of lobe asymmetry, prevalence of high excitation lines in host, radio powers, and environments. Indeed, GRGs are found in both isolated environments and rich clusters.

Broadband radio surveys can provide key insights into the astrophysics occurring at these wavelengths in radio-loud AGN (e.g. Callingham et al. 2017). To model the radio emission and constrain radio jet powers and ages (e.g. Shabala et al. 2008; Turner & Shabala 2015; Hardcastle et al. 2019; Turner et al. 2018a) require surveys with broadband radio data. The ideal region of sky for this work is the Galaxy And Mass Assembly (GAMA, Driver et al. 2009) survey field at RA $\sim 23^h$ and dec. $\sim -32.5°$ (hereafter the 'G23 field') due to its declination and superb multi-wavelength coverage. As part of this effort, the GAMA Legacy Australia Telescope Compact Array (ATCA) Southern Survey (GLASS) is providing deep ($\sim 30\,\mu$Jy/beam RMS) radio observations at 5.5 and 9.5 GHz over G23. As an extension of GLASS, this field has also been observed with the upgraded Giant Metre-wavelength Radio Telescope (uGMRT) as part of the uGMRT/GLASS project at 250–500 and 500–800 MHz.

In this paper, we present the most sensitive radio images of PKS 2250 − 351, a GRG lying in G23, using Australian Square Kilometre Array Pathfinder (ASKAP), uGMRT, ATCA, and the Murchison Widefield Array (MWA). These observations allow us to detect various morphological features, in particular, the diffuse extended emission in the lobes and hotspots. We study the broadband radio properties of PKS 2250 − 351, the multi-wavelength properties of the its host galaxy, its AGN characteristics, and environment. This paper is organised into the following sections. Section 2 presents the radio observations and GAMA data on the host galaxy. In Section 3, we present the modelling and analysis of both the radio data and the host galaxy data. We discuss these results in Section 4 and conclude this work in Section 5. Throughout this paper, we use a flat 'concordance' cosmology of $H_0 = 70$ km s^{-1} and $\Omega_M = 0.3 = 1 - \Omega_\Lambda$. We define radio spectral index, α, by $S_\nu \propto \nu^\alpha$.

2. Observations

2.1. Radio data

Brown and Burns (1991) associated PKS 2250 − 351 with the cluster Abell 3936 and assigned both an estimated redshift from Abell, Corwin, and Olowin (1989). Note all the radio surveys mentioned below (literature and new) use, or are matched to within 1–2% of, the Baars et al. (1977) flux density scale.

2.1.1. Literature radio data

The NRAO VLA Sky Survey (NVSS at 1.4 GHz, Condon et al. 1998) and the Sydney University Molonglo Sky Survey (SUMSS at 0.843 GHz, Bock, Large, & Sadler 1999) images of PKS 2250 − 351 reveal the classic lobe–core–lobe morphology, typical of a resolved radio galaxy. From these images, we observe that it is approximately 5 arcmin in maximum extent. Based upon the spectroscopic redshift of its host, $z = 0.2115$ [from the 2dF Galaxy Redshift Survey (2dFGRS) (Colless et al. 2001, see Section 2.2.1)], this radio source is ≥ 1 Mpc[a] in size. The Tata Institute of Fundamental Research (TIFR) GMRT Sky Survey Alternative Data Release 1 (TGSS ADR1 at $\sim$0.15 GHz, Intema et al. 2017) detects the lobes, and presents faint, uncatalogued emission at the position of the core at 15–20 mJy/beam. The core of PKS 2250 − 351 is detected in the Australia Telescope 20 GHz (AT20G) survey (Murphy et al. 2006) which also provides 5 and 8 GHz measurements. In the AT20G catalogue, this source has a quality flag of 'poor', meaning the flux densities were measured from lower quality data. The radio photometry from NVSS, SUMSS, AT20G, and TGSS is presented in Table 1.

We also use data from the low-frequency GaLactic and Extragalactic All-sky MWA (GLEAM) survey (Wayth et al. 2015) conducted in phase 1 of the MWA (Tingay et al. 2013). The first GLEAM extragalactic data release (hereafter DR1 Hurley-Walker et al. 2017) provides 20 band photometry across 70–230 MHz over a large fraction of the southern sky. Radio sources were detected, and had their flux densities measured, in a deep, high-resolution 170–230 MHz image. Each detected source then had its flux density measured in each of the 20 sub-bands using the positions found in the deep 170–230 MHz image as priors (see Hurley-Walker et al. 2017, for more details). This approach ameliorated the blending of sources at lower frequencies. The two lobes of PKS 2250 − 351 are detected at high significance at 170–230 MHz and their published MWA flux densities are reported in Table 1. Note the corresponding uncertainties have had an 8% systematic uncertainty added in quadrature.

2.1.2. ASKAP early science data

ASKAP (Johnston et al. 2007; McConnell et al. 2016) utilises the revolutionary phased array feeds (PAFs) that densely sample the focal plane of the 12 m antennas with 188 dipoles. To cover the full field of view of the PAF, 36 beams are electronically formed by combining the signals from individual dipoles. Each beam is correlated with the corresponding beam from every other antenna. These data were obtained before the fringes were tracked for each beam (rather than just the centre of the field of view) which results in significant peak flux density suppression for sources near the field edges due to bandwidth smearing.

The G23 field was observed several times during the commissioning and early science period of ASKAP (e.g. Leahy et al. 2019). In this paper, we include data observed on 2018 September 30 with 28 of the final 36 antennas which simultaneously observed 36 primary beams arranged in a square 6×6 footprint as part of Evolutionary Map of the Universe (EMU, Norris et al. 2011) project early science. The total integration time was 11 h with 288 MHz bandwidth centred on 888 MHz.

---

[a]Using 3.45 kpc arcsec^{-1} from astro.ucla.edu/~wright/CosmoCalc.html (Wright 2006).

Table 1. Radio flux densities of the components of PKS 2250–351. The GLASS, ATCA green time, ASKAP and uGMRT data are presented here for the first time. The other data here come from AT20G (Murphy et al. 2010), NVSS (Condon et al. 1998), SUMSS (Bock, Large, & Sadler 1999), GLEAM DR1 (Hurley-Walker et al. 2017), and TGSS ADR1 (Intema et al. 2017). The extended lobe emission seen in the ASKAP and uGMRT images was determined by summing the flux density over an irregular polygon measured on the ASKAP image (see text for more details). For the higher resolution GLASS data, we present the flux densities of just the hotspots as the lobes are resolved out. The columns are: radio telescope used, survey the data are from, the component measured depending on resolution and brightness sensitivity, the observed frequency, the bandwidth, then the flux density (with uncertainty[f]) of the east lobe, core, west lobe, and the total flux.

Telescope	Survey	Component	Frequency (GHz)	$\Delta(\nu)$ (MHz)	East Lobe (mJy)	Core (mJy)	West lobe (mJy)	Total (mJy)
ATCA	AT20G	Compact	20	512	$< 22^a$	57 ± 2	$< 22^a$	—
	Green Time	Extended	9.5	2 000	22.1 ± 1.2	66.2 ± 3.3	10.7 ± 0.6	96.6 ± 3.4
ATCA	GLASS	Compact	9.5	2 000	2.2 ± 0.8	61.9 ± 1.3	1.4 ± 0.5	—
	—	Lobe–compact	9.5	2 000	19.9 ± 1.4	—	9.3 ± 0.8	—
ATCA	AT20G[b]	Compact	8.0	128	—	88 ± 6	—	88 ± 6
	Green Time	Extended	5.5	2 000	38.7 ± 2.1	71.4 ± 3.6	23.6 ± 1.4	134 ± 49
ATCA	GLASS	Compact	5.5	2 000	4.4 ± 1.5	66.3 ± 5.6	3.5 ± 1.2	—
	—	Lobe–compact	5.5	2 000	34.3 ± 2.6	—	20.1 ± 1.8	—
ATCA	AT20G[b]	Compact	5.0	128	—	60 ± 4	—	60 ± 4
VLA	NVSS	Total	1.4	42	135 ± 5	50.0 ± 2.2	100.1 ± 3.8	285 ± 29
ASKAP	EMU	Total	0.888	288	193 ± 26	n/a^c	145 ± 17	> 338
MOST	SUMSS	Total	0.843	3	175.1 ± 5.8	64 ± 5.6	153.8 ± 7.5	393 ± 41
uGMRT	GLASS	Total	0.675	200	237 ± 17	45 ± 3	182 ± 12	464 ± 29
	GLASS	Total	0.323	200	523 ± 68	28 ± 3	438 ± 48	989 ± 91
			0.200^d	61.44	767 ± 62	—	644 ± 53	$1 410 \pm 82$
			0.227	7.68	671 ± 57	—	562 ± 50	$1 232 \pm 76$
			0.220	7.68	690 ± 58	—	578 ± 51	$1 268 \pm 77$
			0.212	7.68	730 ± 61	—	592 ± 52	$1 322 \pm 80$
			0.204	7.68	743 ± 62	—	639 ± 55	$1 382 \pm 83$
			0.197	7.68	755 ± 62	—	613 ± 52	$1 368 \pm 81$
			0.189	7.68	770 ± 64	—	661 ± 56	$1 432 \pm 85$
			0.181	7.68	791 ± 66	—	670 ± 57	$1 461 \pm 87$
			0.174	7.68	844 ± 70	—	735 ± 62	$1 579 \pm 93$
MWA	GLEAM DR1	Total	0.166	7.68	873 ± 72	—	711 ± 60	$1 584 \pm 93$
			0.158	7.68	956 ± 78	—	751 ± 63	$1 708 \pm 100$
			0.151	7.68	979 ± 80	—	800 ± 67	$1 779 \pm 104$
			0.143	7.68	$1 038 \pm 85$	—	889 ± 74	$1 927 \pm 113$
			0.130	7.68	$1 069 \pm 90$	—	914 ± 79	$1 983 \pm 120$
			0.122	7.68	$1 145 \pm 97$	—	974 ± 85	$2 119 \pm 129$
			0.115	7.68	$1 264 \pm 107$	—	$1 025 \pm 89$	$2 289 \pm 139$
			0.107	7.68	$1 378 \pm 118$	—	$1 144 \pm 101$	$2 522 \pm 155$
			0.099	7.68	$1 483 \pm 127$	—	$1 199 \pm 106$	$2 682 \pm 165$
			0.092	7.68	$1 531 \pm 131$	—	$1 301 \pm 114$	$2 832 \pm 174$
			0.084	7.68	$1 725 \pm 147$	—	$1 436 \pm 125$	$3 162 \pm 193$
			0.076	7.68	$1 870 \pm 165$	—	$1 550 \pm 143$	$3 420 \pm 218$
GMRT	TGSS ADR1	Total	0.1475	16.7	721 ± 72	$<20^e$	629 ± 63	$<1 379 \pm 166$

[a] The MWA uncertainties include an additional 8% to account for the overall flux calibration.
[b] 2σ upper limits from 20GHz image provided by P. Hancock (private communication).
[c] Note AT20G images at 5 and 8GHz are not available so there are no constraints on the lobes at these frequencies
[d] It is not possible to determine the core flux density in the ASKAP image due to bandwidth smearing.
[e] 0.2GHz MWA flux determined from wide-band (170-230 MHz) image. The other MWA photometry uses the position in the wide-band image as a prior (see §2.1.1).
[f] Estimated upper limit from visual inspection of image (see §2.1.1).
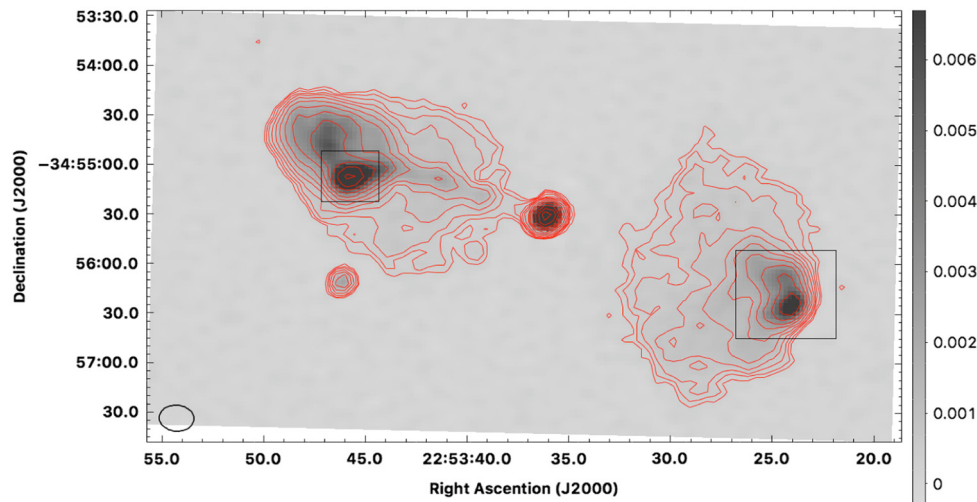
Figure 1. Greyscale image of PKS 2250–351 from our 888 MHz ASKAP continuum data. The local RMS is $\sim$64 μJy/beam and the restoring beam has a full-width half maximum of 10.55 arcsec $\times$7.82 arcsec (indicated in the lower left). The greyscale is a linear stretch in Jy/beam as indicated by the colour bar. The red contours start at 4σ and increase by factors of $\sqrt{2}$. The two black rectangles indicate the regions of the GLASS data presented in Figure 2. The core is clearly identified as well as hotspots positioned on top of diffuse emission from the lobes. Within the eastern lobe, the jet is observed with several knots. The total angular size is 5.66 arcmin ($\equiv$ 1.17 Mpc[1]) with equal lobe lengths. However, the width of each lobe is markedly different with the western lobe being 1.4$\times$ wider than the eastern lobe.

The data were processed using the `ASKAPsoft` pipeline[b] on the Galaxy supercomputer hosted by the Pawsey Supercomputing Centre. The data for each of the 36 beams were bandpass and flux calibrated by observing the primary calibrator source PKS B1934$-$638 at the centre of each primary beam for approximately 3 min. The bandpass was then solved using the Reynolds (1994) model and the solutions were applied to the science target observations. Images for each beam were produced independently in parallel by gridding the visibility data using the `WProject` ASKAPsoft gridder then deconvolving the dirty images with the `BasisfunctionMFS` clean solver, an improved version of the `MultiScale` algorithm available in `CASA` (McMullin et al. 2007). Two iterations of phase-only self-calibration were performed: the first used only a single delta function scale and included only detected components at $>20\sigma$ in the calibration model. The second iteration also used a single delta function scale, but with a lower component threshold of 8σ. The self-calibration solutions were then applied to the data and a final image was produced for each beam using three deconvolution scales: 0 (i.e. the delta function), 15, and 30 pixels. All 36 individual beam images were then combined using a linear mosaic algorithm that corrects for the primary beam attenuation and combines the images using a weighted average.

In Figure 1, we present the continuum image of a cutout around PKS 2250 $-$ 351 from these data. This image nicely reveals the bright hotspots located on top of diffuse lobe emission and it also highlights the eastern jet. The high fidelity of the image is due to the superb uv-coverage from a long integration with 36 antennas of ASKAP[c]. The restoring beam used in this image was 10.55 arcsec $\times$ 7.82 arcsec (full width half maximum for an elliptical Gaussian) with a beam position angle (BPA) of 86.8°.

Since PKS 2250 $-$ 351 lies near the field edge, we do not use the flux density for the core as it is highly smeared. However, as flux is conserved, we can measure the total flux of each lobe by summing the flux density in bespoke irregular polygons around each lobe (tracing the approximate 3σ contour and with no sigma-clipping applied). We convert from the image native units of Jy/beam to mJy using the beam size[d] converted to square pixels. Uncertainties are derived from the RMS measured within these polygons multiplied by the square root of the area of the polygon in units of beam size. These flux densities and uncertainties are reported in Table 1.

From the image in Figure 1, we can more accurately estimate the total size to be 5.66 arcmin ($\equiv$ 1.17 Mpc[1], projected size) and find the lobe lengths to be equal.

2.1.3. GLASS radio data

GLASS is targeting this field over six semesters (across 2016–2019) with ATCA and will provide images and catalogues of the G23 survey field at 5.5 and 9.5 GHz. The data were acquired with a 2 GHz bandwidth at both frequencies and with the correlator in 1 MHz mode. ATCA was in a 6 and 1.5 km configuration for 69% and 31% of the time, respectively. The data used here has a restoring beam of 4 arcsec $\times$ 2 arcsec (BPA $= 0°$), and an RMS of $\sim$24 μJy/beam at 5.5 GHz, and 3.4 arcsec$\times$1.7 arcsec BPA $= 0°$ and $\sim$40 μJy/beam at 9.5 GHz. The data were processed in the standard fashion (see the Users Guide[e]) with `MIRIAD` (Sault, Teuben, & Wright 1995) using a method similar to that outlined in Huynh et al. (2015). The phase calibrator was PKS 2254 $-$ 367. The bright, compact, flat-spectrum core of PKS 2250 $-$ 351 is easily detected in GLASS, but the steep-spectrum diffuse lobes are resolved out due to the minimum short baselines of $\sim$100 m ($\equiv$ 3.2 $k\lambda$ at 9.5 GHz) used in GLASS. However, the two hotspots are clearly detected at both frequencies (see Figure 2).

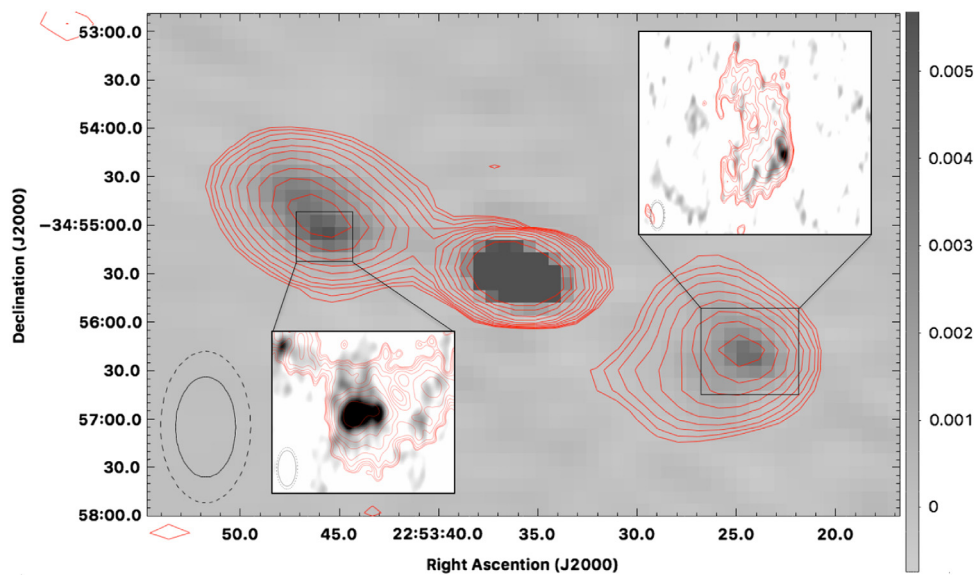We can measure the flux densities of the hotspots using small ellipses and sum up the flux in a similar fashion as with the lobes in

Figure 2. Greyscale ATCA 9.5 GHz images with 5.5 GHz images overlaid as red contours. The contours of the main panel (from the 'green time' data) start at $3 \times \sigma$ (σ=200 μJy/beam). The contours of the inset panels (close-ups of the hotspots from GLASS) start at $3 \times \sigma$ (σ=24 μJy/beam). Both sets of contours increase by factors of $\sqrt{2}$. The resolution is indicated in the lower left of each panel by the ellipses (solid 9.5 GHz and dashed 5.5 GHz). The greyscale stretch of the main figure, indicated by the colour bar, is in Jy/beam. The stretch of the inserts is a linear stretch from -0.2 to +0.3 mJy/beam.

the ASKAP images. The flux densities are converted to mJy and the uncertainties are determined as before, and presented in Table 1.

2.1.4. Additional ATCA observations

As the lobes of this radio source were resolved out in the GLASS observations, we requested ATCA 'green time' observations. We used the same frequencies and bandwidths as GLASS, but in the compact H168 configuration to measure the extended flux densities. These observations were taken on November 31 and 2018 December 1 with about 4 and 6.5 h on source time. The data were reduced in a standard fashion with the MIRIAD software. PKS B1934 − 638 was used to establish an absolute flux density consistent with the Baars et al. (1977) standard as well as to derive our bandpass correction. The data were flagged for radio frequency interference using the guided automated flagging pgflag task. The bandpass was established using the radio spectrum of PKS B1934 − 638 as a reference. The solutions were then copied over to the phase calibrator, PKS 2254 − 367, and a time-dependent phase solution was determined.

Four pointings were used to adequately cover the full extent of PKS 2250 − 351 due to the size of the primary beam at 9.5 GHz. Each pointing was imaged independently using the mfclean task to perform image deconvolution while accounting for the spectral variation of both the synthesised beam and source intensity across the 2 GHz bandwidth. After being primary beam-corrected, these four images were then mosaiced together. We used a Briggs robustness weighting of $R = 0$ at 5.5 GHz and $R = 1$ at 9.5 GHz. In the resultant images, we obtained an RMS of $\sim$0.2 mJy/beam and $\sim$0.1 mJy/beam at 5.5 and 9.5 GHz, respectively. The restoring beams were 46.8 arcsec× 27.8 arcsec (BPA= 79.1°) and 31.0 arcsec× 18.6 arcsec (BPA= 73.5°). We measured the flux densities using the AEGEAN package (Hancock, Trott, & Hurley-Walker 2018) and report these flux densities in Table 1. We conservatively have added in quadrature a 5% absolute flux calibration uncertainty (e.g. the ATCA users guide and Partridge et al. 2016) to the

AEGEAN uncertainties to account for the ATCA absolute flux calibration. We note that the core flux densities measured here with the lower resolution configuration agree well with those measured from the higher resolution GLASS data. The lobe flux densities were derived by subtracting the compact (i.e. hotspot) emission from the total extended flux densities.

2.1.5. uGMRT radio data

Our ongoing campaign to study the G23 field with uGMRT includes data in both band-3 (250–500 MHz) and band-4 (550–850 MHz). In band-3, the survey consists of 50 pointings with each pointing observed for about 30 min in semi-snapshot mode to cover a contiguous 50 deg^2 in total. The band-4 data consists of dedicated pointings of sources of interest in the G23 field with an ON source time of about 1.5 h. The data were recorded with the wideband correlator with 200 MHz bandwidth as well as through the narrow band legacy system (32 MHz bandwidth). The band-4 data were processed using a CASA-based pipeline following procedures appropriate for wideband imaging. For band-3, the wideband data were processed using the CASA-based pipeline and the legacy narrow band data was analysed using the SPAM pipeline (Intema et al. 2009).

PKS 2250 − 351 is near half-power beam width and since the primary beam correction is not well established for the wideband at the time of the analysis, we have used the legacy narrow band data at 325 MHz, instead of the full band-3 for flux measurements. The primary beam correction is applied to each pointing before mosaicing the images from the narrow band legacy system. The band-3 image has a best RMS of $\sim$100 μJy/beam, the legacy 325 MHz image has RMS of $\sim$300 μJy/beam, and the band-4 has RMS of $\sim$22 μJy/beam. The restoring beams are 15.8 arcsec× 6.71 arcsec (BPA= 9.5°) and 7.11 arcsec× 3.59 arcsec (BPA= 23.7°) in band-3 and band-4, respectively (and the restoring beam of the band-3 legacy image is 12.4 arcsec × 8.0 arcsec, BPA= 15°). Since PKS 2250 − 351 is quite bright, it is possible to map the
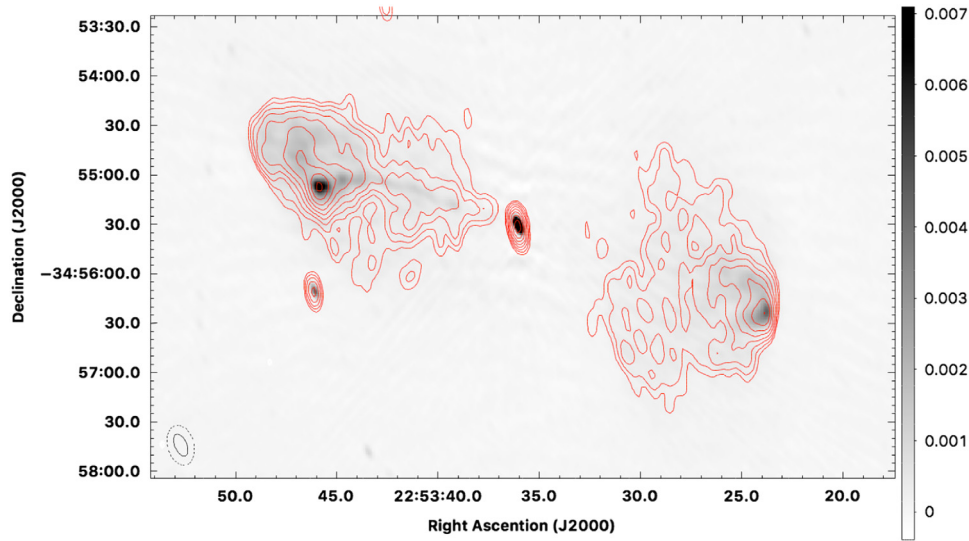
Figure 3. Greyscale image of the band-4 uGMRT image (central frequency 670 MHz). The greyscale stretch in Jy/beam is indicated in the side bar. The red contours of the band-3 legacy data image (central frequency 323 MHz) and start at 2 mJy increasing by $\sqrt{2}$. This image reveals the same structure (the hotspots, diffuse emission, and jet) which we see from the ASKAP image in Figure 1 although does not recover the extended emission quite as well. The restoring beams are shown in the lower left for the band-3 (dashed ellipse) and band-4 (solid ellipse) images.
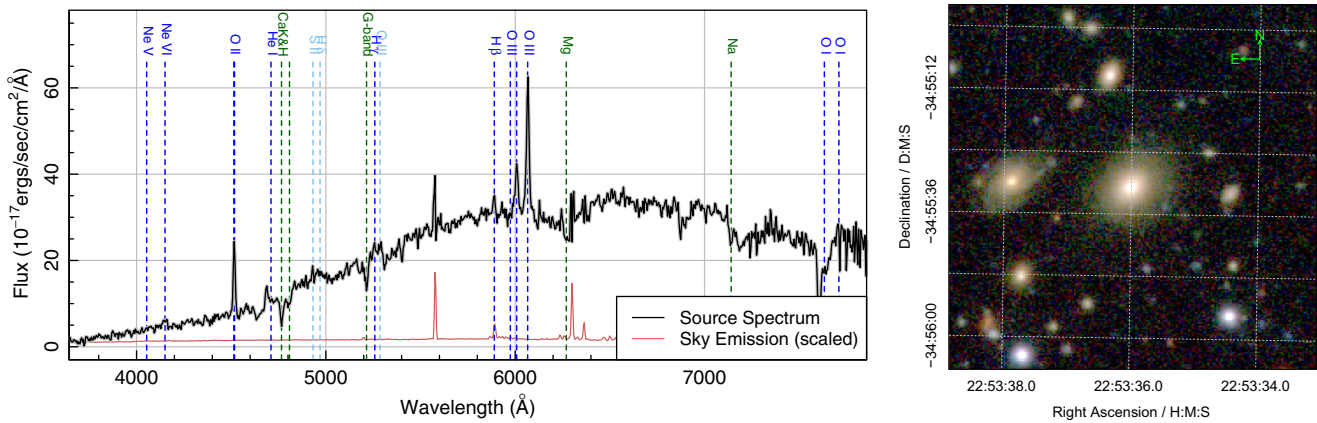
Figure 4. (left) The recalibrated 2 dF spectrum of 2MASS J22533602–3455305. The vertical dashed lines indicate the observed wavelength for spectral lines at z=0.2115 and the emission line ratios are indicative of an AGN (see text for more). (right) A false colour RGB image of the host galaxy of PKS 2250–351 (2MASS J22533602–3455305). The imaging comes from GAMA with g-band (blue), r-band (green), and Z-band (red). The host galaxy appears elliptical in shape showing no signs of disturbance.

features reasonably well. The uGMRT band-4 image is presented in Figure 3 with contours from band-3 overlaid. In band-3, the uGMRT is sensitive to scales up to 32 arcmin, well beyond the size of this GRG.

To measure the lobe fluxes from the uGMRT, we used the same method as we did for the ASKAP data employing the same irregular polygons defined by the ASKAP data. The total flux density and uncertainty were determined in the same fashion using the restoring beams given above. The total flux densities of the lobes and core are presented in Table 1.

2.2. Ancillary data

2.2.1. Literature

From the bright compact radio emission at the core, we find that the host galaxy of PKS 2250 − 351 (see Figures 1 and 3) is 2MASS

J22533602 − 3455305 (Skrutskie et al. 2006). This galaxy has a redshift of $z = 0.2115 \pm 0.0003$ as determined by spectroscopy obtained as part of the 2dF Galaxy Redshift Survey (2dFGRS, Colless et al. 2001). We recalibrated the 2dFRG spectrum so that the r-band magnitude derived from it matches the observed GAMA value, including a correction factor of 3.5 for the 2 arcsec fibre not encompassing the entire extent of the galaxy (Figure 4, right). Its spectrum (see Figure 4, left panel) features prominent narrow [OII] and [OIII] emission lines, but the Hα line is redshifted out of the observed wavelength range.

The observed [O III]λ5007/Hβ line ratio is $\sim$0.9 which is a relatively high value, putting it in the AGN region of [N II]λ6584/Hα v [O III]λ5007/Hβ parameter space (after Baldwin, Phillips, & Terlevich 1981) for almost all values of [N II]λ6584/Hα. The bright [O II] and [O III] lines are narrow ($<$1 000 km/s) which is consistent with this galaxy being an obscured AGN. This spectrum was obtained from a 2 arcsec fibre, smaller than the total extent of

Table 2. The GAMA UV to far-IR photometry of 2MASS J22533602–3455305, the host galaxy of PKS 2250–351. The *WISE* flux densities are converted from Vega magnitudes as explained in the text. PACS and SPIRE (100–500 μm) upper limits are determined from the public H-ATLAS images at 2.5× the local RMS. The columns are: band, effective wavelength and observed flux density with uncertainty.

Band	Effective wavelength (μm)	Flux density (μJy)
u_{VST}	0.3581	21.6 ± 1.9
g_{VST}	0.4760	103 ± 9
r_{VST}	0.6325	380 ± 34
i_{VST}	0.7599	589 ± 52
Z_{VST}	0.8908	743 ± 66
Y_{VISTA}	1.023	951 ± 84
J_{VISTA}	1.256	$1\,184 \pm 104$
H_{VISTA}	1.650	$1\,393 \pm 123$
K_{VISTA}	2.157	$1\,702 \pm 150$
$W1$	3.400	868 ± 49
$W2$	4.652	832 ± 63
$W3$	12.81	1261 ± 424
$W4$	22.38	2050 ± 890
$P100$	98.89	$<5\,250$
$P160$	156.1	$<5\,500$
$S250$	249.4	$<17\,000$
$S350$	349.9	$<13\,750$
$S500$	504.1	$<13\,500$

the galaxy (7–8 arcsec), hence it is perhaps not surprising that the nuclear emission lines dominate this spectrum.

2.2.2. GAMA

The GAMA survey provides *ugriz* optical photometry from the VLT Survey Telescope (VST) and *YJHK* near-IR photometry from the Visible and Infrared Survey Telescope for Astronomy (VISTA) for the G23 field. We present the photometric data of PKS 2250−351 in Table 2 measured by the ProFound software (Robotham et al. 2018). In a *zJK* RGB image (Figure 4), the host galaxy appears extended and elliptical. The upcoming public release of these G23 data will include a cross-matched catalogue of ∼45k high-quality optical spectra.

2.2.3. WISE and Herschel infrared data

The *Wide-field Infrared Survey Explorer* mission (*WISE*, Wright et al. 2010) imaged nearly the entire sky at 3.4, 4.6, 12, and 22 μm. We use the aperture magnitudes of 2MASS J22533602 − 3455305 from the AllWISE catalogue[f] which are more appropriate for a slightly extended source. We then converted these to flux densities presented in Table 2 using the conversion factors from Jarrett et al. (2011) and Brown, Jarrett, and Cluver (2014).

This photometry can be used to derive the following colours: $W1 - W2 = 0.60 \pm 0.04$ and $W2 - W3 = 2.37 \pm 0.32$ (where Wx is the Vega magnitude in band x, and 1–3 corresponds to the 3.4, 4.6, and 12 μm bands, respectively). These colours place the host

galaxy in the region of parameter space typically occupied by AGN (due to the hot dust of the torus heated by the accretion disc, Jarrett et al. 2011; Mateos et al. 2012).

The GAMA survey fields were also covered with far-IR imaging from the *Herschel* Astrophysical Terahertz Large Area Survey (H-ATLAS, Eales et al. 2010). H-ATLAS imaged large areas of the sky using *Herschel's* two imaging instruments [Spectral and Photometric Imaging REceiver (SPIRE) and Photodetector Array Camera and Spectrometer (PACS)[g]]. The observations were obtained in PACS-SPIRE parallel mode in which both instruments are used to image the sky simultaneously. The H-ATLAS south galactic pole observations included the G23 field. Like all the other H-ATLAS observations, data were taken at 100 and 160 μm with PACS and 250, 350, and 500 μm with SPIRE. This source was not detected in any *Herschel* band (confirmed by visual inspection) and we list the 2.5σ upper limits in Table 2.

3. Interpretation and modelling

3.1. Radio morphology

The existence of bright hotspots in the 5.5 and 9.5 GHz seen in the GLASS data (see Figure 2) suggest PKS 2250 − 351 is a Fanaroff and Riley (FR) class II radio galaxy (Fanaroff & Riley 1974), compatible with its total radio luminosity (see Section 3.2.1) although it is unusual in that we observe some asymmetry in the hotspots. Its projected size of 1.17 Mpc classes it as a GRG.

The ASKAP and uGMRT images reveal more detail on the radio galaxy morphology confirming the asymmetric hotspots seen at 5.5 and 9.5 GHz. The bright hotspots on either side are embedded in diffuse emission which is resolved out in GLASS. On the east lobe the diffuse emission extends well past the bright hotspot, whereas on the western lobe the hotspot is at the end. We ascribe the asymmetry seen in the hotspots, jet, and width of the lobes to the environment of this GRG (see Section 3.4). We suggest that the prominence of the eastern jet is not due to beaming as it would imply a jet direction within 10° of the line of sight, and thus an intrinsic size >6.7 Mpc.

3.2. Radio modelling

3.2.1. Radio component SEDs

The broadband radio SEDs of the east and west lobes as, well as the core, are presented in Figure 5 using the data in Table 1. We fit both lobes with a single power-law and a broken power-law model[h] (using a least squares method) and find that the single power-law is significantly preferred (using the Akaike information criterion, corrected for small sample sizes, Akaike 1974; Burnham & Anderson 2002). The two power-laws are $\alpha_{east} = -0.94 \pm 0.01$ and $\alpha_{west} = -1.03 \pm 0.01$ and are plotted in Figure 5. Note that the lobe fluxes have the contributions of the compact emission (i.e. the hotspots) removed at 5.5 and 9.5 GHz. This correction has only a negligible effect on the spectra ($\Delta\alpha \leq 0.03$). The slopes of the lobe SEDs are steep as expected from synchrotron emission originating from an aged population of relativistic electrons with a steep power-law energy distribution.

---

[f]http://wise2.ipac.caltech.edu/docs/release/allwise/.

[g]SPIRE is described in Griffin et al. (2010) and PACS in Poglitsch et al. (2010).
[h]The break frequency between the power-law slopes was left as a free parameter.
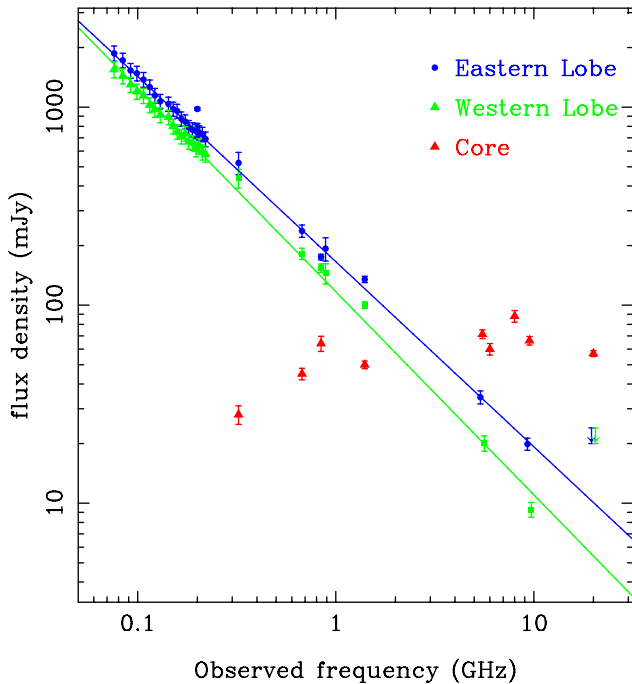
Figure 5. The radio (70 MHz to 20 GHz) SEDs of the core and each lobe of PKS 2250–351 as indicated in the insert. The lobe SEDs (with the contribution of the hotspots subtracted) are well parameterised as a single power-law with the best fits overlaid: α_{east}=-0.94 ± 0.01 and α_{west}=-1.03 ± 0.01.

The uncertainties on these spectral indices are probably underestimated due to some correlation between the MWA flux densities (see Callingham et al. 2017, for a full discussion). By eye one might argue that there is weak evidence for the west lobe becoming steeper above 1 GHz, but it is possible that some extended emission is still resolved out even with the lower resolution ATCA observations. Hence, we conclude that the spectral indices of each lobe are consistent within our overall uncertainties of their value.

The compact lobe components measured from the GLASS data allow us to determine the two-point spectral (5.5–9.5 GHz) indices of the hotspots. We find values of $\alpha_{east}^{hs} = -1.27 \pm 0.90$ and $\alpha_{west}^{hs} = -1.68 \pm 0.91$. While these values are steeper than those for the lobes, they are consistent with the lobe values within the uncertainties. The hotspots are still detected in the lowest frequency, high-resolution radio image at 323 MHz from the uGMRT (see Figure 3). However, the resolution is ∼4 times worse compared to the GLASS images. Hence, it is difficult to quantify the contribution of the hotspots to the lobes at low frequency. The hotspots could conceivably contribute a larger fraction of the total flux at lower frequencies, but equally we might expect the hotspots to become synchrotron self-absorbed (SSA) at some low frequency.

The spectrum of the unresolved core appears fairly flat above ∼1 GHz as expected from the classical assumption of the superposition of many separate synchrotron components each with different turnover frequencies due to SSA.

There is some suggestion of a downturn at low frequencies from the uGMRT data which is further suggested by the faint emission seen in TGSS (see Section 2.1.1). However, we cannot tell with these data if this is due to SSA or free–free absorption processes. The AT20G 8 GHz flux density is a little higher than the other measurements, but as it was observed near-simultaneously

with the 5 GHz data we put this down to measurement scatter or genuine variability of the core.

Using the lobe spectral indices for the *k*-correction, we find a total luminosity at 1.4 GHz (151 MHz) of $L_{1.4\text{GHz}} = 3.24 \pm 0.25 \times 10^{25}$ W Hz-1 ($L_{151\text{MHz}} = 2.70 \pm 0.11 \times 10^{26}$ W Hz-1) consistent with PKS 2250 − 351 being an FR II source as determined from the observations of hotspots (see Figure 1).

3.2.2. Jet kinetic power and source age

We use observations of the symmetric western lobe to infer jet kinetic power and source age using the Radio AGN in Semi-analytic Environments (RAiSE) dynamical model (Turner & Shabala 2015; Shabala et al. 2017; Turner et al. 2018a; Turner, Shabala, & Krause 2018b). We refer the interested reader to those papers for a comprehensive description of our modelling approach. Briefly, we produce luminosity-size tracks and optically thin synchrotron radio continuum spectra, for a wide range in jet kinetic power. While in some sources it is possible to infer the lobe magnetic field strength from the break in the synchrotron spectrum (Turner et al. 2018b), we find no break in the spectral energy distribution (SED) of PKS 2250 − 351 (Figure 5) and hence we adopt a value of 0.3 times the equipartition field. This is characteristic of FR II lobe field strengths measured through inverse-Compton observations (Croston et al. 2017). Modelled jets consist of a pair plasma (i.e. no protons), and we use the observed low-frequency spectral index to constrain the initial particle spectral index at the hotspots, $\alpha_{\text{inj}} = -0.6$. The injection spectral index is related to the power-law index in energy (*s*) as $\alpha_{\text{inj}} = \frac{-(s-1)}{2}$. Thus, the α_{inj} value we use corresponds to $s = -2.2$ which is consistent with expectations from diffusive shock acceleration (e.g. Heavens & Drury 1988). The lobes have a steeper spectrum than this α_{inj} most likely due to energy losses (Turner et al. 2018b).

Backflow of accelerated plasma from the hotspots inflates the radio cocoon, which expands supersonically through the intracluster gas. RAiSE models the dynamics of lobe expansion (radially and transverse), and accounts for synchrotron, adiabatic, and inverse-Compton losses from the emitting electrons. We run a grid of models for environments corresponding to group centre galaxies in haloes hot intra-cluster medium (ICM) with mass spanning $3 \times 10^{13} - 3 \times 10^{14}$ M$_\odot$; we consider these to be representative upper and lower limits of the (unknown) ICM conditions in the outskirts of Abell 3936. We then used maximum likelihood to find the best-fitting jet kinetic powers and dynamical ages. Regardless of environment, we consistently recover a total (i.e. for both jets) lobe-derived jet power of $Q_{\text{jet}}^{\text{lobe}} = 1 - 1.5 \times 10^{38}$ W, and ages of 260–320 Myr. These values do not change appreciably even if we relax our assumptions about the magnetic field. This age is quite large compared to other GRGs (Ishwara-Chandra & Saikia 1999) and even 'old' regular radio-loud AGN (Murgia et al. 2011).

Lobe dynamics trace time-averaged jet power, which may not be directly comparable with the (quasi-instantaneous) accretion rate determined through mid-IR observations. Godfrey and Shabala (2013) presented a method for calculating the instantaneous[i] jet power from observations of hotspots; this method has been shown to be consistent with time-averaged dynamical jets powers (Shabala & Godfrey 2013) with some scatter, as expected. We obtain a hotspot-derived jet power of $Q_{\text{jet}}^{\text{hs}} \sim 8 \times 10^{36}$ W for

---

[i]Assuming the jet has a velocity of ∼0.7 *c*, the time it takes to reach the hotspots is a few Myr, much shorter than the age of the lobes.
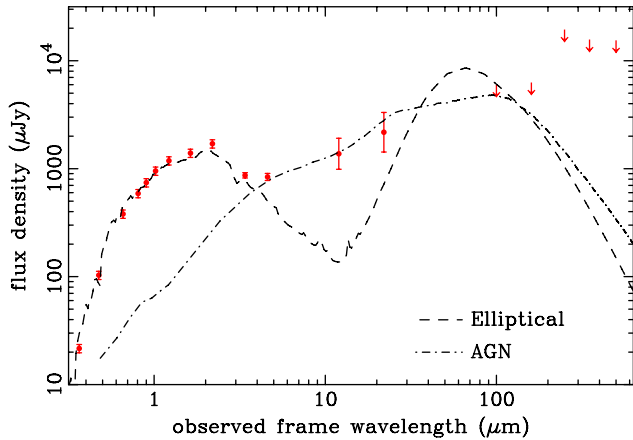
Figure 6. We plot the UV to far-IR SED of 2MASS J22533602–3455305, the host galaxy of PKS 2250–351, with the data from Table 1. We show the best fit stellar SED model (dashed line) to these data (excluding the three longer wavelength *WISE* bands which are dominated by the AGN). We overlay an AGN model (dash-dot line) from Symeonidis et al. (2016) to demonstrate how it dominates the *WISE* bands.

each jet, i.e. 1.5×10^{37} W in total, an order of magnitude lower than the time-averaged lobe-derived jet power. We suggest some plausible explanations for this interesting discrepancy in the discussion (Section 4.3) below.

3.3. The host galaxy

The radio emission from the bright compact core is unambiguously associated with the galaxy 2MASS J22533602 − 3455305. Its morphology and colours indicate it would normally be a 'red and dead' massive elliptical. From Figure 4, it appears the major axis is close to perpendicular to the radio jet axis, a feature which is common in elliptical hosts of radio galaxies (Battye & Browne 2009).

3.3.1. SED modelling

We fit the UV to far-IR SED using the `ProSpect`[j] code. The `ProSpect` code fits stellar libraries for different populations and dust templates to observed data. The IR emission from the dust is balanced by the absorption fitted to the optical/UV photometry assuming a uniform screen. As the three longer wavelength *WISE* bands are dominated by the AGN (as indicated by the *WISE* colours, see Section 2.2.1), we do not use them in the fitting of the stellar components. To account for the non-detections in the *Herschel* bands, we use a range of flux values from 0 to 2.5 σ, i.e. input flux densities of $1.25 \pm 1.25\,\sigma$ (where σ is the image RMS). The SED is best fit with an old stellar population which had a peak star formation rate (SFR) around 5 Gyr ago.

We find the galaxy has a negligible current SFR of $\ll 0.5\,M_\odot$ yr^{-1} and a stellar mass of $1.93 \pm 0.07 \times 10^{11}\,M_\odot$. This fit is shown in Figure 6 where the *Herschel* bands are shown as 2.5σ upper limits. We overlay an AGN template from Symeonidis et al. (2016) to demonstrate the AGN dominance in the *WISE* bands. In comparison to the general population of galaxies, these values put this galaxy far below the SFR/stellar mass 'main sequence' (Brinchmann et al. 2004; Noeske et al. 2007; Seymour et al. 2008) with a specific SFR of $<< 1 \times 10^{-2}$ Gyr^{-1} (i.e. 'red and dead').

The non-detections in the far-IR from the *Herschel Space Observatory* (see Table 2) imply an upper limit to the 60 μm luminosity of $L_{60\,\mu m} \lesssim 1 \times 10^{10}\,L_\odot$ which corresponds to a SFR $\lesssim 2\,M_\odot$ yr^{-1} (using the relationship from Calzetti et al. 2010) and are therefore consistent with the low reported SFR. The host galaxy is also undetected in the relatively shallow *ROSAT* all-sky X-ray survey (Voges et al. 1999) and has yet to be targeted by other X-ray facilities.

3.3.2. Black hole accretion rate

The *WISE* colours and luminosity, along with the optical spectrum, are all consistent with ongoing obscured accretion onto a SMBH and with the lack of star formation indicated by the UV to near-IR SED. Hence, the *WISE* photometry can be used to estimate a mid-IR luminosity and infer an accretion rate. Interpolating between the $W2$ and $W3$ flux densities (assuming a power-law), we can measure the 5 μm rest-frame luminosity as $\nu L_{5\mu m} = 1.560 \pm 0.16 \times 10^{10}\,L_\odot$ in solar luminosities. This is around an order of magnitude below the knee of the low-redshift luminosity function of mid-IR selected AGN (Lacy et al. 2015). Following the conversion factor of 10 from Lacy et al. (2015), we find $L_{BOL}^{AGN} = 1.56 \pm 0.16 \times 10^{11}\,L_\odot$.

We also estimate the bolometric AGN luminosity from the [O III]λ5007 line. We measured an [O III]λ5007 flux of $1.3 \pm 0.3 \times 10^{-15}$ erg s^{-1} cm^{-2} which corresponds to a luminosity of $L_{O III}\lambda5007 = 3.4 \pm 0.9 \times 10^7\,L_\odot$. Following Heckman et al. (2004), we convert to a bolometric AGN luminosity by multiplying by a factor of $\sim$3 500 ($\pm$0.38 dex), thus obtaining $L_{BOL}^{AGN} = 1.2 \pm 0.3 \times 10^{11}\,L_\odot$. This value is consistent with the mid-IR derived AGN luminosity and we take the mean of these values ($L_{BOL}^{AGN} \sim 1.38 \pm 0.18 \times 10^{11}\,L_\odot$) in our deliberations below (where the uncertainty is taken from the range of the two values).

The efficiency of black hole accretion in AGN is not strongly constrained, but is estimated to be between 6% and 40% (see discussion in Section 6 of Drouart et al. 2014). Here we conservatively take a value of 10%, but note it can vary. Using this value, we obtain an accretion rate of $\sim$0.1 $M_\odot$ yr^{-1}. We can compare this value to the Eddington accretion rate which depends on black hole mass.[k] We estimate the mass of the black hole from the mass of the host galaxy assuming it lies on the local M–σ relation (e.g. Ferrarese & Merrit 2000; Kormendy & Ho 2013). Specifically, we use the stellar mass reported above as the bulge mass, as our host appears to be a pure elliptical, and the conversion to black hole mass quoted in Häring and Rix (2004). We therefore estimate a black hole mass of $M_{BH} = 3.3 \pm 0.8 \times 10^8\,M_\odot$ (where the uncertainty comes from that in the conversion equation of Häring & Rix 2004) which we can use to determine an Eddington luminosity of $\sim$1 $\times$ 10$^{13}\,L_\odot$. Hence, our estimated Eddington accretion rate is $\lambda_{EDD} \sim \frac{1.4 \times 10^{11}}{1 \times 10^{13}} \sim 0.014 \pm 0.004$ where the uncertainty is propagated from those of the black hole mass and bolometric AGN luminosity.

3.4. Environment

PKS 2250 − 351 has been associated with the 'Irregular' cluster Abell 3936 (by Brown & Burns 1991) with an Abell count of 95 and richness of '2'. We investigate this association using a galaxy group catalogue (included as part of the forthcoming G23 field

<hr/>

[j]https://github.com/asgr/ProSpect.

[k] $\frac{L_{EDD}}{L_\odot} = 3.2 \times 10^4 \left(\frac{M}{M_\odot} \right)$, where M is the mass of the SMBH.
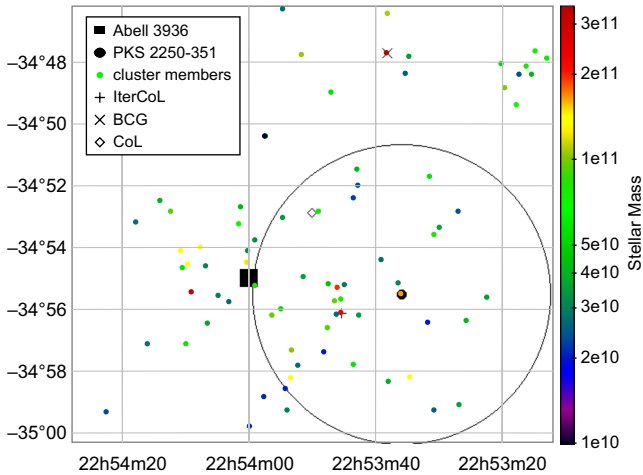
Figure 7. Sky distribution of spectroscopically confirmed GAMA sources lying at $0.207 \le z \le 0.2180$ (i.e. $\Delta(cz) \le 1\,500$ km s^{-1}). PKS 2250–351 is indicated by a larger black dot surrounded by a 1 Mpc radius circle. The large black square is the Abell cluster position and the '+', 'X', and diamond indicate three different estimates of the cluster centre from the GAMA group catalogue. The colour code of the galaxies indicate their stellar masses. The radio galaxy lies to the west of our most confident estimate of the cluster centre, the Iterative Centre of Light (IterCoL).

data release) based on a friends-of-friends algorithm following the method of Robotham et al. (2011). This group catalogue was produced with the ~45k high-quality spectroscopic redshifts in G23 and includes information such as the number of members, the virial mass, and three separate estimates of the group centres. These centres are based on a centre of light (CoL) method, an iterative centre of light method (IterCoL), and the brightest cluster galaxy (BCG).

We confirm 2MASS J22533602 − 3455305 as a member of the largest group in G23 at the reported position of Abell 3936 (see Figure 7). This group has 92 spectroscopic members (including 2MASS J22533602 − 3455305) and an estimated virial mass of $9.7 \pm 1.0 \times 10^{14}\,M_\odot$. This mass estimate is based on the observed velocity dispersion (705 ± 50 km s^{-1}) and the estimated cluster radius. Note the uncertainty in the mass is from the velocity dispersion and does not include that on the cluster radius. However, the number of members and virial mass estimate strongly suggest that this is a massive cluster at $z = 0.213$ (a higher redshift than estimated by Brown & Burns 1991).

In Figure 7, we plot the spatial distribution of the spectroscopically confirmed galaxies in the range $0.207 < z < 0.218$ (i.e. within $\Delta(cz) = 1,500$ km s^{-1} of the cz of 2MASS J22533602 − 3455305). For reference, we indicate a circle of radius 1 Mpc around PKS 2250 − 351. The colour bar indicates the estimated stellar masses of the galaxies (determined as described in Section 3.3.1). The three group centre estimates from the group catalogue are indicated as shown in the legend. The results of these three methods differ significantly.

The IterCoL estimate lying due east of PKS 2250 − 351 is probably the best if one were to make a judgement from the distribution of galaxies in Figure 7. The CoL method is further north, drawn in that direction by the distribution of the galaxies in a filament that runs through the whole G23 field. The BCG estimate is clearly a long way off for this structure. Hence, we conclude that PKS 2250 − 351 is a member of Abell 3936, but ~1 Mpc west of its centre.

4. Discussion

4.1. The host galaxy

For the first time, we have identified the radio source PKS 2250 − 351 with the host galaxy 2MASS J22533602 − 3455305, a massive elliptical at $z = 0.2115$. It has a negligible SFR but prominent mid-IR emission due to accretion onto the SMBH. The AGN emission is highly obscured in the UV and optical, consistent with the central engine being obscured by a torus structure viewed from approximately side-on and with the standard unification of AGN by orientation (Urry & Padovani 1995).

4.2. Jet power and ages

Our estimate of the age of radio source is relatively well defined. PKS 2250 − 351 is an FR II with well-defined bow shocks, so we know it must still be expanding supersonically (and was expanding faster in the past). For a cluster sound speed of 1 000 km s^{-1} (~1 kpc/Myr, Sarazin 1988), this places a pretty strong upper limit on the age of $\sim(600/M_{lobe})$ Myr where M_{lobe} is the average external Mach number of the lobe-driven bow shock (w.r.t. the ICM) over the lifetime of the source.

If the radio source is not in the plane of the sky (i.e. is larger), this would imply a larger age. The jet power would then also need to be adjusted appropriately. We can estimate the angle of the jet relative to the line of sight using (2) of Hardcastle, Lawrence, and Worrall (1998) which relates the jet-to-counterpart flux ratio to the angle between the jet and the line of sight. Using the ASKAP image and comparing the measured flux in parts of the jet away from knots with an equidistant position on the opposite (western) side, we obtain a brightness ratio of 3. Assuming a jet spectral index of $\alpha_{jet} = -0.5$ (from the canonical $s = -2$ electron energy power-law index from first-order Fermi acceleration processes) and a jet speed of $\beta = 0.7$[1], this flux density ratio is equivalent to 74° to the line of sight (i.e. close to side-on).

Our assumptions also depend on magnetic field strength. We took the typical particle to magnetic field energy density ratio from inverse-Compton observations of Hardcastle and Croston (2010). Lower magnetic field strengths require a higher jet power to obtain the same radio luminosity—and hence younger age, to match the size constraint. Changing the magnetic field by a factor of 3 (i.e. the magnetic field energy density by a factor of 10, now consistent with lobes at equipartition) changes the best fit jet power by 0.2 dex (giving a broader range of $1 - 2.5 \times 10^{38}$ W), and increasing the age range by 30 Myr (giving a range of 230–320 Myr).

4.3. Jet power vs accretion rate

Our results in Section 3.2.2 present a possibly conflicting scenario with different jet power estimates. The lobe-derived estimate of the jet power is an order of magnitude greater than the hotspot-derived value. This difference is right at the limit of the scatter seen between instantaneous jet power estimates from hotspots and the time-averaged dynamic jet powers (Shabala & Godfrey 2013). However, that scatter applies to younger and smaller radio galaxies where one might expect the instantaneous and time-averaged values to agree more closely. On the assumption that the change in jet power we observe is real, we consider other possibilities.

---

[1]This is a lower limit considering that the FR II jets must be substantially supersonic and the sound speed is $\sim \frac{1}{3}c$.

Firstly, the AGN accretion rate (and therefore jet power) is simply varying over the age of the radio galaxy. While simulations by Novak, Ostriker, and Ciotti (2011) have demonstrated rapid, $\ll$ 1 Myr, variability at low Eddington accretion rates, simulations by Gaspari, Ruszkowski, and Oh (2013) have shown that 'chaotic cold accretion' (CCA) can lead to variable accretion rates. In this picture, condensation of hot intracluster gas and subsequent inelastic collisions of cold gas clouds remove angular momentum, raining cold clouds onto the super-massive black hole at rates significantly in excess of the Bondi rate; this generates the powerful jets averaged over this stochasticity. Mechanical feedback from the jets then truncates the cooling process, and the jets are powered by the (less efficient) standard cold, TD. A testable prediction of this CCA hypothesis is the existence of old filamentary gas structures in the vicinity of the AGN host.

Another possibility for the drop in jet power over the life time of the radio source could be a change in accretion state. Our estimated Eddington accretion rate of $\lambda_{\mathrm{EDD}} = 0.014 \pm 0.004$ is around the value at which accretion onto black holes switches from an inefficient, advection-dominated thick disc accretion flow (ADAF, Fabian & Rees 1995) to an efficient TD accretion flow. An ADAF is more efficient than a TD at producing jets (e.g. Meier 2002), hence the higher average power derived from the lobes could have occurred in this ADAF mode. Then as the accretion rate gradually increases, the state of the accretion disc switches to the efficient TD mode and the power of the jet drops by an order of magnitude. This is consistent with the relationships between jet power and accretion rate presented in Meier (2002) which give a jet power around an order of magnitude lower for a TD compared to an ADAF (for the same mass, accretion rate, and spin).

4.4. Environment

PKS $2250 - 351$ resides in what is likely a massive cluster, Abell 3936 (with an estimated virial halo mass of $9.7 \pm 1 \times 10^{14} \, \mathrm{M}_\odot$ from its velocity dispersion). It is not uncommon to find GRG in such environments (Komberg & Pashchenko 2009). However, to exist at all in such an environment this radio galaxy must have a powerful jet and be long-lived, as is supported by our modelling of the radio lobes in Section 3.2.

Abell 3936 is not detected in cluster surveys with *ROSAT* (e.g. Böhringer et al. 2013) to a level of $1.8 \times 10^{-12} \, \mathrm{erg \, s^{-1} \, cm^{-2}}$ from 0.1 to 2.4 keV. At the redshift of Abell 3936, this flux is equivalent to a luminosity of $2.34 \times 10^{44} \, \mathrm{erg \, s^{-1}}$. Using equation 10 of Böhringer et al. (2013)[m], the *ROSAT* non-detection implies a mass $\leq 5.5 \times 10^{14} \, \mathrm{M}_\odot$ (with a 30% uncertainty). This discrepancy between the 'virial' mass and the X-ray mass upper limit could be explained if the cluster was not yet relaxed.

This assertion is supported by the observation that the group catalogue does not provide a clear determination of a cluster centre with different estimates providing different positions (see Figure 7). From our analysis in Section 3.4, it seems that PKS $2250 - 351$ is probably to the west of the densest grouping of galaxies eastern lobe pointing roughly towards it. While the ICM in this case maybe not be as dense as for a virialised cluster, it likely increases towards this galaxy concentration. Hence, the western radio lobe expands outwards more easily as the density of the ICM

decreases, while the eastern lobe is more confined by an increasingly dense ICM. This idea is further supported by the difference in the lobe flux densities. A lobe expanding into a less dense environment will have a lower luminosity for the same jet power, which is consistent with the eastern lobe being $\sim 30 - 100\%$ brighter than the western lobe.

The prominence of the jet in the eastern lobe is curious. It could partly be explained by the increasingly dense ICM into which it is drilling. The knots and kinks seen in the eastern jet could possibly be due to hydrodynamical instabilities. We note that it is unlikely to be due to relativistic beaming which would require a small angle, $\ll 10°$, between the jet motion and the line of sight, inconsistent with our earlier estimate of $74°$. We can also rule out precession due to the asymmetry of the lobe.

The jet and lobe asymmetry could be due to a more complex morphology (e.g. a wide-angled tail radio source) viewed in projection, but this is also in contradiction with our determination that this radio galaxy is close to side-on. Future polarimetric observations with ASKAP may better constrain the orientation of PKS $2250 - 351$. If one radio lobe is expanding into a denser part of the ICM, one might expect it to have a higher rotation measure due to the denser foreground plasma.

Future X-ray observations (e.g. by *eROSITA*) will provide additional clues on these issues, potentially providing evidence of the interaction of the radio lobes with the ICM.

5. Conclusions

We have completed a detailed study of the giant radio galaxy PKS $2250 - 351$, its host galaxy and environment. This work demonstrates how we can improve our understanding of radio-loud AGN using broadband radio surveys (i.e. from MWA, uGMRT, ASKAP, and ATCA) with high-quality multi-wavelength surveys such as GAMA. In future papers, this work can be extended to much larger samples of radio sources in the G23 field. By comparing the instantaneous and past averaged jet powers with the current accretion rate, we can begin to determine when and how jets form in SMBHs.

The primary results from this work are:

- We have confirmed the association of the GRG PKS $2250 - 351$ at $z = 0.2115$ with the large, but irregular Abell 3936 cluster. This cluster is likely unrelaxed and has no clear centre, although PKS $2250 - 351$ lies to the west of the highest concentration of galaxies.

- Its host galaxy, 2MASS J22533602 $- 3455305$, confirmed here for the first time, is a massive, 'red and dead' elliptical well below the SFR/stellar mass main sequence.

- The O III emission line and *WISE* photometry imply a current AGN bolometric luminosity of $1.38 \pm 0.18 \times 10^{11} \, \mathrm{L}_\odot$ ($\equiv 0.1 \, \mathrm{M}_\odot \, \mathrm{yr}$-1 accretion rate). This AGN activity is highly obscured in the UV and optical. We estimate a black hole mass of $3.3 \pm 0.8 \times 10^8 \, \mathrm{M}_\odot$ (from the local M–σ relation) and hence an Eddington accretion rate of $\lambda_{\mathrm{EDD}} = 0.014 \pm 0.004$, a value close to the transition between an accretion disc in an ADAF state and a TD state.

- The lobe-derived jet power is an order of magnitude greater than the hotspot-derived jet power. Given the hotspots trace the much more recent accretion (a few

---

[m]This relationship assumes no evolution in the relationship between X-ray luminosity and cluster temperature.

Myr) and the age of the radio emission is quite old (260–320 Myr), we suggest that the accretion disc may have changed state over this period. We propose that initially this radio galaxy was in an inefficient, ADAF mode which explains the high, average jet power estimated from the lobes. With an increase in accretion rate, the radio galaxy then switched to a TD mode, which explains the lower, current jet power estimated from the hotspots, but also the high current accretion rate seen in the host.

- The asymmetry of the lobe widths may possibly be due to a density gradient in the ICM with the less luminous lobe expanding more widely into a less dense environment. However, without deeper X-ray observations, it is not possible to accurately determine the location and position of the centre of the cluster Abell 3936 relative to PKS 2250−351.

References

Abell, G. O., Corwin, H. G. JR, & Olowin, R. P. 1989, ApJS, 70, 1
Akaike, H. 1974, IEEE Trans. Autom. Control, 19, 716
Baars, J. W. M., Genzel, R., Pauliny-Toth, I. I. K., & Witzel, A. 1977, A&A, 61, 99
Baldwin, J. A., Phillips, M. M., & Terlevich, R. 1981, PASP, 93, 5
Battye, R. A., & Browne, I. W. A. 2009, MNRAS, 399, 1888
Bock, D. C.-J., Large, M. I., & Sadler, E. M. 1999, AJ, 117, 1578
Böhringer, H., Chon, G., Collins, C. A., Guzzo, L., Nowak, N., & Bobrovskyi, S. 2013, A&A, 555, A30
Brinchmann, J., Charlot, S., White, S. D. M., Tremonti, C., Kauffmann, G., Heckman, T., & Brinkmann, J. 2004, MNRAS, 351, 1151
Brown, D. L., & Burns, J. O. 1991, AJ, 102, 1917
Brown, M. J. I., Jarrett, T. H., & Cluver, M. E. 2014, PASA, 31, e049
Burnham, K. P., & Anderson, D. R. 2002, Model Selection and Multimodel Inference: A Practical Information-Theoretic Approach (2nd edn.; New York: Springer-Verlag), https://www.springer.com/gp/book/9780387953649
Callingham, J. R., et al. 2017, ApJ, 836, 174
Calzetti, D., et al. 2010, ApJ, 714, 1256
Colless, M., et al. 2001, MNRAS, 328, 1039
Condon, J. J., Cotton, W. D., Greisen, E. W., Yin, Q. F., Perley, R. A., Perley, G. B., Taylor, G. B., & Broderick J. J. 1998, AJ, 115, 1693
Croston, J. H., Ineson, J., Hardcastle, M. J., & Mingo, B. 2017, MNRAS, 470, 1943
Driver, S. P., et al. 2009, Astron. Geophys., 50, 5.12
Drouart, G., et al. 2014, A&A, 566, A53
Eales, S., et al. 2010, preprint arXiv:1005.2189
Fabian, A. C., & Rees, M. J. 1995, MNRAS, 277, L55
Fanaroff B. L., & Riley, J. M. 1974, MNRAS, 167, 31P
Fender, R. P., Belloni, T. M., & Gallo, E. 2004, MNRAS, 355, 1105
Ferrarese, L., & Merrit, D. 2000, ApJ, 539, L9
Gaspari, M., Ruszkowski, M., & Oh, S. P. 2013, MNRAS, 432, 3401
Godfrey, L. E. H., & Shabala, S. S. 2013, ApJ, 767, 12
Griffin, M. J., et al. 2010, preprint arXiv:1005.5123
Hancock, P. J., Trott, C. M., & Hurley-Walker, N. 2018, PASA, 35, e011
Hardcastle, M. J., & Croston, J. H. 2010, MNRAS, 404, 2018
Hardcastle, M. J., Lawrence, C. R., & Worrall, D. M. 1998, ApJ, 504, 743
Hardcastle, M. J., et al. 2019, A&A, 622, A12
Häring, N., & Rix H.-W. 2004, ApJ, 604, L89
Heavens, A. F., & Drury, L. O. 1988, MNRAS, 235, 997
Heckman, T. M., & Best, P. N. 2014, ARA&A, 52, 589
Heckman, T. M., Kauffmann, G., Brinchmann, J., Charlot, S., Tremonti, C., & White, S. D. M. 2004, ApJ, 613, 109
Hurley-Walker, N., et al. 2017, MNRAS, 464, 1146

Huynh, M. T., Bell, M. E., Hopkins, A. M., Norris, R. P., & Seymour, N. 2015, MNRAS, 454, 952

Intema, H. T., van der Tol, S., Cotton, W. D., Cohen, A. S., van Bemmel, I. M., & Röttgering, H. J. A. 2009, A&A, 501, 1185

Intema, H. T., Jagannathan, P., Mooley, K. P., & Frail, D. A. 2017, A&A, 598, A78

Ishwara-Chandra, C. H., & Saikia, D. J. 1999, MNRAS, 309, 100

Jarrett, T. H., et al. 2011, ApJ, 735, 112

Johnston, S., et al. 2007, PASA, 24, 174

Komberg, B. V., & Pashchenko I. N. 2009, ARep, 53, 1086

Kormendy, J., & Ho, L. C., 2013, ARA&A, 51, 511

Krause, M. G. H., et al. 2019, MNRAS, 482, 240

Kuźmicz, A., Jamrozy, M., Bronarska, K., Janda-Boczar, K., & Saikia D. J. 2018, ApJS, 238, 9

Lacy, M., Ridgway, S. E., Sajina, A., Petric, A. O., Gates, E. L., Urrutia, T., & Storrie-Lombardi, L. J. 2015, ApJ, 802, 102

Leahy, D. A., et al. 2019, PASA, 36, e024

Mateos, S., et al. 2012, MNRAS, 426, 3271

McConnell, D., et al. 2016, PASA, 33, e042

McMullin, J. P., Waters, B., Schiebel, D., Young, W., & Golap, K. 2007, ASPC, 376, 127

Meier, D. L. 2002, NewAR, 46, 247

Merloni, A., Heinz, S., & di Matteo, T. 2003, MNRAS, 345, 1057

McHardy, I. M., Koerding, E., Knigge, C., Uttley, P., & Fender, R. P. 2006, Nature, 444, 730

Murgia, M., et al., 2011, A&A, 526, A148

Murphy, E. J., et al. 2006, ApJ, 651, L111

Murphy, T., et al. 2010, MNRAS, 402, 2403

Noeske, K. G., et al. 2007, ApJ, 660, L43

Norris, R. P., et al. 2011, PASA, 28, 215

Novak, G. S., Ostriker, J. P., & Ciotti, L. 2011, ApJ, 737, 26

Partridge, B., López-Caniego, M., Perley, R. A., Stevens, J., Butler, B. J., Rocha, G., Walter, B., & Zacchei, A. 2016, ApJ, 821, 61

Poglitsch, A., et al. 2010, A&A, 518, L2

Rees, M. J. 1978, Nature, 275, 516

Reynolds, J. E. 1994, Technical report, A Revised Flux Scale for the AT Compact Array. ATNF, Epping

Robotham, A. S. G., et al. 2011, MNRAS, 416, 2640

Robotham, A. S. G., Davies, L. J. M., Driver, S. P., Koushan, S., Taranu, D. S., Casura, S., & Liske, J. 2018, MNRAS, 476, 3137

Sarazin, C. L. 1988, X-ray Emission from Clusters of Galaxies. Cambridge Astrophysics Series (Cambridge: Cambridge University Press)

Sault, R. J., Teuben, P. J., & Wright, M. C. H. 1995, in Astronomical Data Analysis Software and Systems IV, R. A. Shaw, H. E. Payne, & J. J. E. Hayes, eds., Astronomical Society of the Pacific Conference Series, Vol. 77, 433 (arXiv:astro-ph/0612759)

Seymour, N., et al. 2008, MNRAS, 386, 1695

Shabala, S. S., & Godfrey L. E. H. 2013, ApJ, 769, 129

Shabala, S. S., Ash, S., Alexander, P., & Riley, J. M. 2008, MNRAS, 388, 625

Shabala, S. S., Deller, A., Kaviraj, S., Middelberg, E., Turner, R. J., Ting, Y. S., Allison, J. R., & Davis, T. A. 2017, MNRAS, 464, 4706

Skrutskie, M. F., et al. 2006, AJ, 131, 1163

Symeonidis, M., Giblin, B. M., Page, M. J., Pearson, C., Bendo, G., Seymour, N., & Oliver, S. J. 2016, MNRAS, 459, 257

Taylor, M. B. 2005, ASPC, 347, 29

Tingay, S. J., et al. 2013, PASA, 30, e007

Turner, R. J., & Shabala, S. S. 2015, ApJ, 806, 59

Turner, R. J., Rogers J. G., Shabala, S. S., & Krause, M. G. H. 2018a, MNRAS, 473, 4179

Turner, R. J., Shabala, S. S., & Krause, M. G. H. 2018b, MNRAS, 474, 3361

Urry, C. M., & Padovani, P. 1995, PASP, 107, 803

Voges, W., et al. 1999, A&A, 349, 389

Wayth, R. B., et al. 2015, PASA, 32, e025

Wright, E. L. 2006, PASP, 118, 1711

Wright, E. L., et al. 2010, AJ, 140, 1868